USM3D Simulations for the Third AIAA Sonic Boom Prediction Workshop*

Alaa Elmiligui[1], Mohagna J. Pandya[2], and Melissa B. Carter[3]
NASA Langley Research Center, Hampton VA 23681

Boris Diskin[4]
National Institute of Aerospace, Hampton, VA 23666

Sudheer N. Nayani[5]
Analytical Services & Materials, Inc., Hampton, VA 23666

The NASA USM3D flow solver was used to compute test cases for the Third AIAA Sonic Boom Prediction Workshop (SBPW3). The test cases included a nearfield biconvex shock-plume interaction wind tunnel model and the C608 Low Boom Flight Demonstrator. Numerical simulations were conducted on the mixed-element and tetrahedral grids provided by the workshop committee, as well as a family of grids generated by an in-house approach known as BoomGrid. The nearfield pressure signatures were extracted and propagated to the ground, and the perceived loudness levels on the ground were computed. The USM3D nearfield pressure signatures, corresponding ground signatures, and loudness levels on the ground were compared with that of mean values from other workshop participants. The effect of three flux-limiters on the accuracy of nearfield pressure signature prediction was investigated and results were compared with that of mean values from other workshop participants. The effect of using wall-function models for predicting nearfield pressure signatures was also evaluated. Results showed that the overpressure signatures extracted from

[1] Research Engineer, Configuration Aerodynamics Branch, Mail Stop 499, AIAA Senior Member.
[2] Aerospace Engineer, Configuration Aerodynamics Branch, Mail Stop 499, AIAA Senior Member.
[3] Aerospace Engineer, Configuration Aerodynamics Branch, Mail Stop 499, AIAA Associate Fellow.
[4] Sr. Research Fellow, National Institute of Aerospace, Hampton, VA, AIAA Associate Fellow.
[5] Senior Scientist, CFD Group, 107 Research Drive, AIAA Associate Fellow.

the wall-modeled simulations and the wall-resolved simulations are in good agreement. The use of wall functions (wall-modeled simulations) allowed for approximately 23% savings in the time to solution and yielded comparable perceived loudness levels on the ground to the wall-resolved Reynolds-averaged Navier Stokes simulations.

Nomenclature

C_p	=	pressure coefficient
$\Delta P/P_\infty$	=	overpressure ratio, $(P - P_\infty)/P_\infty$
H	=	distance below model, feet
H/L	=	dimensionless distance below model
L	=	model length, feet
M_∞	=	freestream Mach number
P_∞	=	freestream static pressure, psi
P_o	=	Total Pressure, psi
P_o/P_∞	=	Engine plenum total pressure ratio to freestream static pressure
Re	=	freestream unit Reynolds number, 1/in
T_∞	=	freestream static temperature, °R
T_o	=	total temperature, °R
T_o/T_∞	=	Engine plenum total temperature ratio to freestream static temperature
X	=	longitudinal coordinate, inch
y^+	=	dimensionless distance from the wall measured in terms of viscous lengths
α	=	angle of attack, deg.
δ_1	=	height of first cell in a grid
φ	=	off-track azimuthal angle, deg.
∞	=	ambient, or freestream flow conditions

Acronyms

AIAA	=	American Institute for Aeronautics and Astronautics
BC	=	Boundary Condition
BL	=	Body length

BG	=	BoomGrid
C608	=	NASA low boom flight demonstrator
CFD	=	Computational Fluid Dynamics
CPU	=	Central Processing Unit
dB	=	decibels
ECS	=	Environment Control System
GridTool	=	Interactive grid/geometry setup tool
IGES	=	Initial Graphics Exchange Specification file format
HANIM	=	Hierarchical Adaptive Nonlinear Iteration Method
LaRC	=	Langley Research Center
LBPW	=	Low Boom Prediction Workshop
LBFD	=	Low boom flight demonstrator
LCASB	=	Loudness Code for Asymmetric Sonic Booms
NPR	=	Nozzle Pressure Ratio
PL	=	Perceived level metric of loudness, dB
RANS	=	Reynolds-averaged Navier Stokes
RBOS	=	Retroreflective background oriented schlieren
SA	=	Spalart-Allmaras turbulence model
SBPW	=	Sonic Boom Prediction Workshop
STEP	=	Standard for the Exchange of Product Data
TetrUSS	=	Tetrahedral Unstructured Software System
USM3D	=	Unstructured tetrahedral Mesh 3D RANS solver
USM3D-ME	=	Mixed-element USM3D solver
VGRID	=	Unstructured grid generation program
WF	=	Wall function

I. Introduction

The first Low Boom Prediction Workshop (LBPW1) was held in January 2014 in conjunction with the AIAA Science and Technology Forum and Exposition (SciTech). A summary and statistical analysis of the LBPW1 is given

in Ref. [1]. The workshop focused on three configurations: an axisymmetric body with a flat-top ground signature, a simple nonlifting wing body with N-wave signature, and a complex configuration with wing, tail, flow-through nacelles, and blade mount sting (LM-1021). Details of all three configurations can be found on the LBPW1 webpage [2]. The low boom workshop website has the listing of workshop participants and their presentations [2]. A follow up special session was held at AIAA AVIATION Forum 2014 where presenters and LBPW1 participants documented their findings [3]. LBPW1 configurations captured a range of geometric complexities and were significantly louder than the expected future supersonic aircrafts. The perceived loudness (PL) of the axisymmetric body was approximately 92 dB, the nonlifting wing body PL was approximately 96 dB, and the LM-1021 PL was 84-94 dB. The LM1021 had larger scatter in PL than the axisymmetric body and the nonlifting wing body.

In January 2017, the AIAA Applied Aerodynamics Technical Committee (APATC) conducted their second Sonic Boom Workshop (SBPW2) during the AIAA Science and Technology Forum and Exposition (SciTech 2017) to build on the success of the LBPW1. The SBPW2 was a two-day event, the first day focused on the nearfield simulation and the second day included both the nearfield simulation and the atmospheric propagation methods. The SBPW2 committee provided three required and one optional nearfield CFD test cases [4]. The test cases were an axisymmetric equivalent area body (AXIE), a JAXA wing body (JWB) [5], and a NASA low boom supersonic configuration, C25D [6], with flow-through nacelle (C25D-F) and with propulsive engine boundary conditions (C25D-P). The surface definition of all four test cases were designed to generate, at three body lengths, similar on-track nearfield pressure signatures. A summary and statistical analysis of the SBPW2 participants' results were presented in a follow up AIAA session that was held during the AIAA 2017 AVIATION Forum [8]. The SBPW2 test cases produced quieter ground loudness levels than the LBPW1 test cases and were more representative of future supersonic aircraft designs.

In January 2020, APATC conducted the third Sonic Boom Workshop (SBPW3) during the SciTech 2020. The complexity of the SBPW3 test cases was increased to include the NASA C608 low boom flight demonstrator (LBFD) prototype and a biconvex shock-plume interaction wind tunnel model. Details of both configurations can be found on the SBPW3 webpage [10]. The two-part workshop covered both the prediction of nearfield sonic boom signatures with CFD, as well as propagation of the nearfield pressures to the ground. The objectives of the workshop were to assess the state-of-the-art computational methods as practical aerodynamics tools for predicting nearfield pressure signatures for industry relevant geometries; and to identify areas needing additional research and development. The workshop was attended by over 50 individuals and had 23 participants who represented 6 different countries and 18

organizations that included government, industry, and academia. A summary and statistical analysis of the SBPW3 participants' results were presented in four special sessions during AIAA SciTech 2021 [11].

In the recent study, the NASA Tetrahedral Unstructured Software System TetrUSS [24] with its USM3D flow solver was used to compute flowfields for the biconvex shock-plume interaction in the wind tunnel and the C608 configuration. TetrUSS has served as a reliable computational aerodynamic analysis tool for the U.S. Government and Industry for over 2 decades. The legacy Navier-Stokes flow solver within TetrUSS, USM3D, is based on a fully tetrahedral cell-centered discretization. Recently, Pandya et al. [25], extended USM3D capability to handle mixed-element grids composed of hexahedral, prismatic, pyramidal, and tetrahedral cells, in a new version of USM3D, called the mixed-element USM3D version (USM3D-ME). The extension of USM3D for multiple grid topologies has enabled its application and verification via code-to-code comparison on a wide variety of problems for which structured hexahedral grids and solutions are readily available. Using a new nonlinear iteration methodology, USM3D-ME was able to reduce time to solution up to a factor of 70 on benchmark three-dimensional turbulent flow problems [26]. Leveraging efficient parallelization, the USM3D-ME has been applied to compute solutions on grids up to 1.5 billion cells and up to 14,000 grid partitions [28]. USM3D-ME is currently being used within the NASA Commercial Supersonic Technology project, Low Boom Flight Demonstration project, and the Advanced Air Transport Technology project with the Transonic Truss-Braced Wing. The synergistic advancements to USM3D-ME have improved its accuracy and iterative and parallel efficiency providing a positive impact on the applied aerodynamicists' workflow.

The first objective of the present paper is to document USM3D-ME simulations for the SBPW3 test cases The second objective is to access wall function (WF) formulations for predicting the C608 nearfield pressure signatures. WF models allow for a significant reduction of the grid size and in computer resources to achieve converged solution.

This paper is organized as follows: (1) description of the SBPW3 test cases; (2) brief description of TetrUSS and USM3D-ME; (3) description of numerical grids used in the study; (4) presentation of the numerical results and comparison with SBPW3 participants mean results; and (5) summary of the work and the relevant findings.
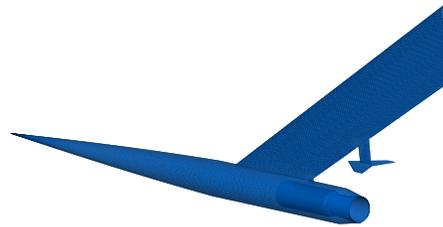
II. Sonic Boom Workshop Test Cases

The nearfield pressure field was analyzed for the biconvex and C608 configurations. The biconvex shock-plume interaction model, referred to as the biconvex model in the rest of this paper, was part of a wind tunnel test conducted at the NASA Ames Research Center (ARC) Unitary Plan Wind Tunnel (UPWT) 9- by 7-Foot Supersonic Wind Tunnel

(9x7 SWT). The wind tunnel test was designed to provide a high-quality dataset for CFD validation. The objective of the test was to investigate the interactions between a supersonic jet plume and shock and expansion waves produced by various shock-generating surfaces. Details of the wind tunnel test can be found in Refs. [29-30]. Figure 1a shows a photograph of the model tested in the wind tunnel while Fig. 1b shows the schematic of the model used in the current numerical study. The SBPW3 technical committee provided the biconvex geometry in both IGES and STEP file format. The nose is located at (x,y,z) = (0,0,0) and the model is at 3° incidence. The biconvex numerical simulations were conducted for a freestream Mach number of 1.4, unit Reynolds number of 376,850 per inch, and static temperature of 374 °R.
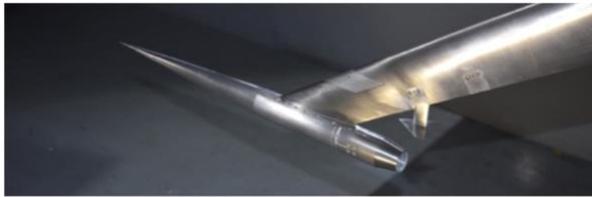
(a) Photograph of the biconvex model in NASA Ames 9x7 wind tunnel   **(b) Schematic of biconvex model**

Figure 1 Biconvex shock plume interaction model.

The C608 LBFD configuration was the SBPW3 second test case. The C608 configuration is an earlier version of NASA/X-59 LBFD configuration [31]. The C608 configuration is more complex in terms of geometry and propulsion boundary conditions than the biconvex model. Figure 2 shows a schematic of the C608 configuration. The SBPW3 technical committee provided the C608 geometry in both IGES and STEP file format. The nose is located at (x,y,z) = (0,0,0) and the geometry included a rotation about the nose of 2.15° to include design angle of attack. The C608 configuration has a length of 1080 inch. The horizontal stabilator is at an incidence of +3.1° and the t-tail is at an incidence of +5.2° and aileron deflection is 0.5°. The C608 numerical simulations were conducted for a Mach number of 1.4 and at conditions corresponding to an altitude of 53,200 ft.

(a) Image of NASA/X-59 LBFD, Ref. [19]   (b) Schematic of C608 model

Figure 2 Schematic of NASA X-59 LBFD.

III. Computational Techniques

In this section, the details of the numerical approach and the computational grids used by USM3D to compute the flowfield for the SBPW3 test cases are presented.

A. USM3D Flow Solver

USM3D is the Navier-Stokes flow solver used in the current study. USM3D was developed at the NASA Langley Research Center (LaRC). USM3D has served as a reliable computational aerodynamic analysis tool for U.S. government and Industry for over 2 decades. The preceding versions of USM3D were customized for only the tetrahedral grids. Unfortunately, the diagonal faces and skewed topology of the highly stretched tetrahedra result in a severely distorted spatial differencing stencil for computing fluxes, which may adversely affect the near-wall flow solution. Recently, USM3D has been extended to support the solutions on mixed-element grids that provide improved numerical simulation using flow-aligned anisotropic hexahedral or prismatic cells in a boundary layer and isotropic tetrahedral cells away from a boundary layer. Furthermore, additional algorithmic capabilities have been implemented that significantly improved solver robustness and time to solution. In this study, the new mixed-element USM3D code will be referred to as USM3D-ME.

A new solution methodology named Hierarchical Adaptive Nonlinear Iteration Method (HANIM) has been implemented in the USM3D-ME [27]. HANIM is a strong nonlinear method that improves the robustness, efficiency, and automation of the Reynolds-averaged Navier-Stokes (RANS) solutions. HANIM provides two additional hierarchies around the simple preconditioner of USM3D-ME, which is based on a linearization of a simplified discrete formulation and a point-implicit Gauss-Seidel (G-S) relaxation scheme. The HANIM hierarchies are a matrix-free

linear solver for the exact linearization of the RANS equations and a nonlinear control of the solution update. The goal of these hierarchies is to enhance the iterative scheme with a mechanism for an automatic adaption of the operational pseudotime step to increase convergence rates and overcome transitional instabilities and limit cycles. The matrix-free linear solver uses the Fréchet derivatives and a Generalized Conjugate Residual method. A further enhancement to the efficiency of USM3D-ME HANIM is achieved by implementing a line-implicit preconditioner. Line-implicit iterations simultaneously update a preconditioner solution at all cells of a grid line. A line-generation algorithm suitable for general unstructured grids is developed that is solely based on local grid connectivity [28].

USM3D-ME has been parallelized for maximizing the CFD solution throughput. The parallelization is based on a Message Passing Interface (MPI) paradigm. The grid decomposition is performed internally following the current state of the art. Interpartition communication is performed judiciously and efficiently such that excellent strong scalability and weak scalability are achieved. Strong scalability is a measure of the efficiency a parallel flow solver has on a given grid when the partition size is gradually reduced, employing progressively more grid partitions. Weak scalability is a measure of how well a parallel flow solver is able to sustain its parallel efficiency when partition size is kept constant while grid size and the number of grid partitions are increased at the same rate.

Several important modifications to the discretization schemes were made to improve USM3D-ME's accuracy, efficiency, and robustness. Some of the modifications include:

1) a fully-implicit formulation that is entirely based on cell-center solutions

2) modification to a nodal-averaging scheme for a viable flow solver parallelization

3) more consistent linearization of the target operator inside the approximate Jacobian used by the USM3D preconditioner

4) an adaptive face-based catastrophic limiter

5) several options for gradient limiters needed for high-speed flows

6) implementation of a numerically more robust version of the negative variant of the Spalart-Allmaras turbulence model (SA-neg) that is commonly used for external aerodynamic problems

7) implementation of a nonlinear quadratic constitutive relationship within the turbulent stress equations to better capture the physics of a flow problem

USM3D-ME allows for various options for computing the inviscid-flux quantities across each cell face. In the current study, the Harten, Lax, and van Leer with contact restoration scheme (HLLC) [32] was used for the inviscid

flux discretization; and three types of limiters namely Barth-Jespersen, Venkatakrishnan, and van Albada limiters were used to suppress numerical oscillations "wiggles" near shocks [33]. The effect of the limiters on nearfield pressure signature will be reported in the results section. The Spalart-Allmaras, one-equation turbulence model (SA-neg) that is commonly used for external aerodynamic problems was used to model turbulence [36].

One of the objectives of this paper was to assess the effect of using WF formulation for predicting the C608 nearfield pressure signatures. At the time of writing this paper, USM3D-ME did not have the WF formulation fully implemented and tested. Hence, the legacy tetrahedral USM3D was used to evaluate the WF RANS simulations. WF RANS simulations require the first grid point off the wall to be in the log-law region of the boundary layer ($25 \leq y+ \leq 250$). A wall function is used to bridge the gap between near wall region and the fully turbulent region away from the wall. The wall-resolved RANS simulations require a higher near-wall grid resolution ($y^+ \leq 1$) to be able to accurately resolve the boundary layer.

B. sBOOM, Ground Propagation Code

The NASA LaRC-developed sonic-boom prediction code sBOOM was used to propagate sonic-boom signatures to the ground. sBOOM solves the augmented Burgers' equation numerically and takes into account effects such as nonlinearity, molecular relaxation, and thermoviscous absorption into the propagation process. The thickness of the shocks is predicted analytically, which avoids artificial smoothing and empirical shock thickening during loudness calculations. sBOOM can predict on-track and off-track ground signatures with or without wind effects, along with consideration for aircraft maneuvers. Further details about sBOOM and its applications can be found in Ref. [38]. In this study, the Mark VII Perceived Loudness Level (PL) [39] was adopted as a measure of loudness at the ground and the NASA Loudness Code for Asymmetric Sonic Booms (LCASB) was used to compute the loudness levels [40].

C. Computational Grids

Two sets of grids were used in this study. The first set included the mixed-element and the tetrahedral grids provided by the SBPW3 committee. The SBPW3 mixed-element grids were comprised of mixed tetrahedra, prisms, and pyramids while the tetrahedral grids comprised of only the tetrahedral cells. The SBPW3 mixed-element and tetrahedral grids were designed to have a $y^+ \leq 1$. The SBPW3 tetrahedral grids were a subdivision of the SBPW3 mixed-element grids and had the same grid nodes.

The second set of grids was generated, in house, for the WF RANS simulations. These grids have the first grid point off the wall in the log-law region of the boundary layer ($25 \leq y+ \leq 70$) and are called WF grids for the rest of the paper. The WF grids were generated to study whether a reduction in time to solution can be achieved by reducing grid size while preserving accuracy in predicting nearfield pressure signatures. The next sections describe the details of the biconvex and C608 grids used in the current study.

1. Biconvex shock plume interaction grids

The SBPW3 committee provided a sequence of mixed-element and tetrahedral grids for the biconvex model. Table 1 provides an overview of the family of mixed-element grids, which is comprised of three grids: coarse, medium, and fine. The biconvex wind tunnel model grids have a uniformly refined spacing in three dimensions and are intended for $\alpha = 0°$. Table 2 provides an overview of the tetrahedral grids. The mixed-element grid size varies from a total of 3.48 million cells on the coarsest grid to 16.03 million on the finest grid while the tetrahedral grid size varies from 4.79 million tetrahedral cells on the coarsest grid to 18.82 million on the finest grid. More details about the grids can be found in Ref. [10]. Figure 3 shows a schematic of the grid distribution for the biconvex coarse grid. USM3D-ME solutions have been computed for all the grids given in Table 1.
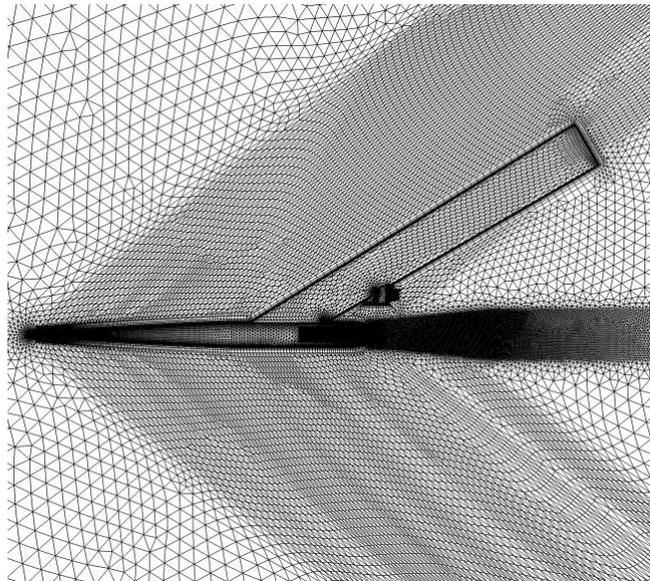

Figure 3 Schematic showing biconvex model grid distribution (coarse grid).

Table 1 SBPW3 biconvex family of mixed-element grids.

Grid Level	Name	Scale Factor	Nodes (millions)	Cell Type (millions)			
				Tetrahedral	Pyramids	Prisms	Total
Bi_ME_3	Coarse	1.57	0.846	2.825	0.004	0.650	3.480
Bi_ME_2	Medium	1.28	1.576	5.985	0.006	0.993	6.985
Bi_ME_1	Fine	1.00	3.286	14.628	0.012	1.388	16.028

Table 2 SBPW3 biconvex family of tetrahedral grids.

Grid Level	Name	Scale Factor	Nodes (millions)	Tetrahedral Cells (millions)
Bi_Tet_3	Coarse	1.57	0.846	4.786
Bi_Tet_2	Medium	1.28	1.576	8.978
Bi_Tet_1	Fine	1.00	3.286	18.816

2. LBFD Grids

The SBPW3 committee provided a sequence of mixed-element and fully tetrahedral grids for the C608 configuration. Table 3 provides statistics for the family of mixed-element grids, while Table 4 provides statistics for the sequence of tetrahedral grids. Each family of grids is comprised of six grids: tiny, coarse, medium, fine, extrafine and superfine. The C608 grids have a uniformly refined spacing in all three dimensions. The angle of attack of 2.15° is designed into the geometry and the nose is set to be at $(x,y,z) = (0,0,0)$. The mixed-element grid size varies from a total of about 30 million cells on the tiny grid level to approximately 400 million cells on the superfine grid level, while the tetrahedral grid sizes vary from about 68 million tetrahedral cells on the coarsest grid to about 965 million cells on the superfine grid level. Figure 4 shows a schematic of the C608 grid distribution. The C608 grid consisted of two parts: the inner grid, which is enclosed by the green line in Fig. 4, and the Mach-cone-aligned outer collar grid. More details about the grids can be found in Ref. [10]. USM3D solutions were provided for the first 5 grid levels of the mixed-element and tetrahedral grids. No solutions were provided for the superfine grid because the solution on the extrafine grid was grid converged.

The WF grids consisted of two parts: a refined inner "core grid" close to the body and a Mach-cone-aligned outer collar grid. The HeldenMesh software package [42] was used to generate the refined inner grid. HeldenMesh is a software system developed by the Helden Aerospace Corporation for the rapid generation of high-quality, three-dimensional, unstructured meshes about complex configurations. The in-house code, Boom Grid (BG) [43], was used to generate the collar grid where cells are aligned to the freestream Mach angle.
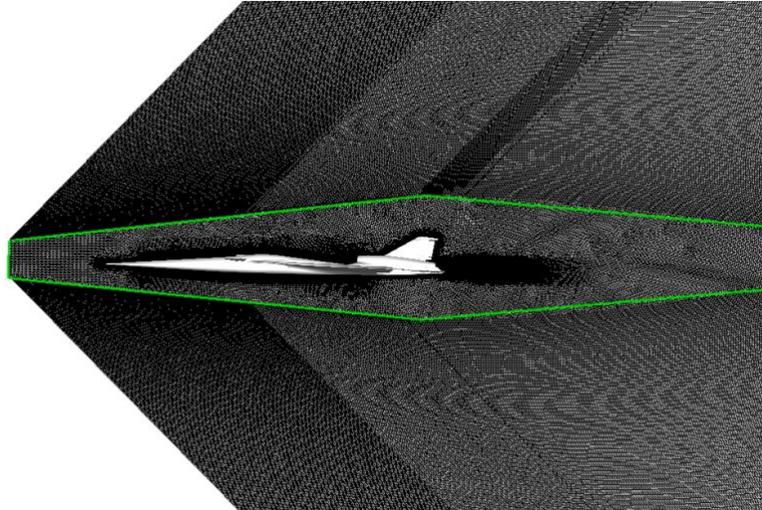
Figure 4 Schematic of the C608 SBPW3 coarse grid.

The transition between the unstructured near-body grid and the Mach-cone-aligned collar grid was made as close to the body as possible. Typically, the outer boundary is placed in such a way that there is a $0.02 \times$ Body Length (BL) clearance between the wing tip and the outer boundary. The first cell in the collar grid was made of similar size to the adjacent core grid cell. Spacing in the radial direction increased geometrically. The collar grid geometric growth rate was scaled logarithmically similar to the boundary layer growth rate. The collar grid was swept at the freestream Mach angle with the vehicle oriented at the intended angle of attack. The collar grid extended 5000 inches from the body to allow for the extraction of signatures at 3 BL or 3240 inches, without interference from the farfield boundary reflections.

Table 5 shows statistics of the WF grids used in the parametric study. The WF grids were designed to have a much larger y^+ (an order of magnitude larger) than the SBPW3 committee grids. The first cell height varied from 0.0001 inches to 0.0235 inches. The grid sourcing was kept the same between all the grids listed in Table 5.

Table 3 C608 family of mixed-element grids.

Grid Level	Name	Scale Factor	Nodes (millions)	Cell Type (millions)		
				Tetrahedral	Prisms	Total
C608_ME_6	Tiny	1.28	11.783	10.600	19.225	29.825
C608_ME_5	Coarse	1	20.701	14.682	35.347	50.028
C608_ME_4	Medium	0.8	34.879	21.267	61.008	82.274
C608_ME_3	Fine	0.64	50.215	36.568	86.084	122.651
C608_ME_2	Extrafine	0.5	89.459	67.139	153.393	220.531
C608_ME_1	Superfine	0.4	162.970	119.457	281.557	401.014

Table 4 C608 family of tetrahedral grids.

Grid Level	Name	Scale Factor	Nodes (millions)	Tetrahedral Cells (millions)
C608_Tet_6	Tiny	1.28	11.783	68.487
C608_Tet_5	Coarse	1	20.701	121.015
C608_Tet_4	Medium	0.8	34.879	204.706
C608_Tet_3	Fine	0.64	50.215	295.276
C608_Tet_2	Extrafine	0.5	89.459	527.865
C608_Tet_1	Superfine	0.4	162.970	964.797

Table 5 C608 tetrahedral grids used in wall-function study.

Grid Level	First Cell Height (inch)	Nodes (millions)	Tetrahedral Cells (millions)	y^+
C608_WF_4	0.0223	33.08	197	70
C608_WF_3	0.0159	33.85	199	50
C608_WF_2	0.0069	34.90	205	25
C608_WF_1	0.0001	38.74	228	< 1

D. Boundary Conditions

The Riemann-invariant boundary condition is used along the farfield boundaries of the computational domain. The supersonic inflow boundary condition is used at the domain inflow plane and the extrapolation boundary condition was used at the downstream outflow plane of the computational domain. The no-slip viscous boundary condition is used on all solid surfaces. The symmetry boundary condition is applied at the symmetry plane of both configurations. A subsonic jet boundary condition was applied at nozzle/exhaust faces [44]. The subsonic jet boundary condition is determined from user-prescribed values for total pressure, P_{0jet}, and total temperature, T_{0jet}. The reference quantities, the freestream conditions, and the engine boundary conditions that are utilized in the numerical simulations of the flowfield around the biconvex and the C608 are provided in Table 6 and Table 7, respectively.

Table 6 Freestream and boundary conditions for the biconvex model.

M_∞	1.6
α	0° (grid provided includes rotation about the nose of 3°)
T_∞	**374** °R
Re	376,850 per inch
Plenum P_o/P_∞	8.0
Plenum T_o/T_∞	1.768

Table 7 Freestream and boundary conditions for the C608.

M_∞	1.4
α	0° (grid provided includes rotation about the nose of 2.15°)
T_∞	389 °R
Re	109,776 per inch
Engine fan face P/P_∞	2.8 (or alternatively M = 0.4)
Engine plenum P_o/P_∞	10.0
Engine plenum T_o/T_∞	7.0
ECS inlet face P/P_∞	1.4 (or alternatively M = 0.35)
Engine bay vent P_o/P_∞	2.4
Engine bay vent T_o/T_∞	2.0
L	1080 inches
Cruise Altitude	53,200 (ft)

Figure 5 shows a schematic view of the biconvex model showing the nozzle body, biconvex tail, jet boundary patch and wind tunnel probes. The jet boundary patch is colored in red in Fig. 5. Figure 6 shows the C608 power boundary conditions. The total pressure, P_{0jet}, and total temperature, T_{0jet}, values are prescribed for the engine bay ventilation face and the engine plenum face. The engine bay ventilation face is the crescent shape shown in yellow in Figure 6a while the engine plenum face is shown in red. The boundary conditions for the engine fan face and Environment Control System (ECS) are prescribed as either a constant static pressure or constant Mach number and are shown in red in Figure 6b. The effect of using the constant static pressure boundary condition versus a constant Mach number is presented in Section IV.

Biconvex Tail

Wind Tunnel
Total Pressure
Probe

Plenum BC
$P_o/P_\infty = 8.0$
$T_o/T_\infty = 1.768$

Wind Tunnel
Total Temperature
Probe
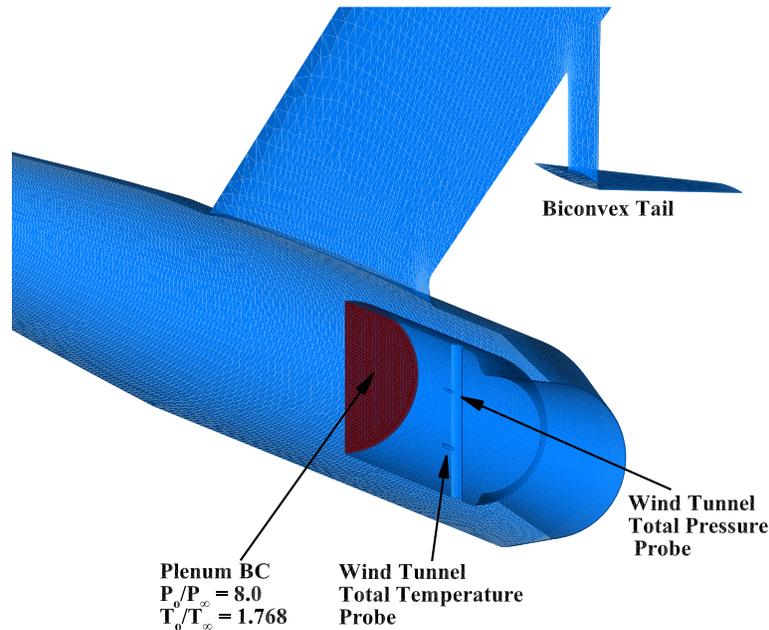
Figure 5 Schematic showing the biconvex model nozzle body, biconvex tail, jet boundary patch and wind tunnel probes.

(a)   (b)
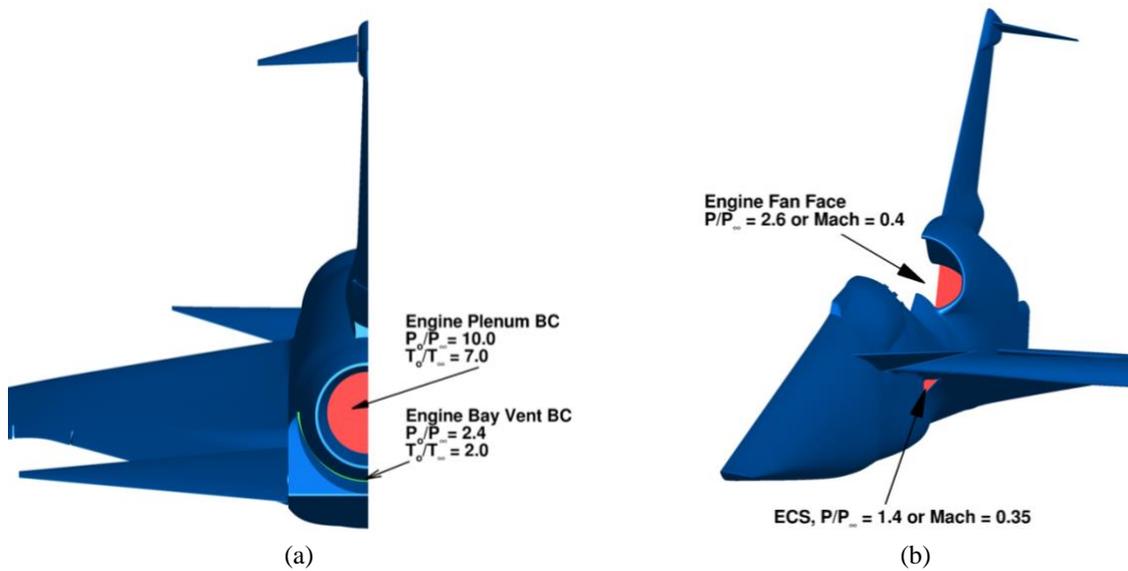
Figure 6 Schematic showing C608 power boundary conditions.

IV. Results and Discussion

In this section, USM3D-ME results for the SBPW3 test cases are presented and discussed. The biconvex simulations are presented first followed by the C608 simulations. The nearfield pressure signatures presented in this section represent the overpressure ratio, which is a dimensionless parameter that describes the relative pressures throughout the flowfield and is defined as $\Delta P / P_\infty = (P - P_\infty) / P_\infty$. The Barth-Jespersen limiter is used, unless otherwise mentioned. Effect of limiters on the nearfield pressure signature is discussed later in this section.

A. The Biconvex Shock-Plume Interaction Wind Tunnel Model

The numerical simulations for the flowfield around the biconvex model are performed without tunnel walls, for a freestream Mach number of 1.6 and a unit Reynolds number of 376,850 per inch. The nearfield pressure signatures are extracted at distances of 15 inches away from the configuration and at three off-track angles, φ, of 0°, 15°, 30°. Figure 7 shows the Bi_Tet_1 symmetry plane colored with USM3D-ME density gradient contours. The black line depicts the location of the extracted pressure signatures, 15 inches away from the model. Lines of constant density gradient extend to the farfield boundary. The USM3D-ME simulations capture the main features of the flowfield around the biconvex model, including the nose bow shock, plume shear layer, nozzle lip shock, biconvex leading and trailing shocks, as well as the refraction of the trailing biconvex shocks as they pass through the plume. Figure 8 compares the USM3D-ME results on the Bi_Tet_1 grid with the wind tunnel retroreflective background oriented

schlieren (RBOS) image taken at the 9x7 SWT [29]. Figure 8 shows good agreement between the flow characteristics observed in the RBOS images and USM3D-ME density gradient contours. The grid in the wake region of the biconvex wing is coarse and hence current simulations fail to accurately capture the wake that is visible in the RBOS image.
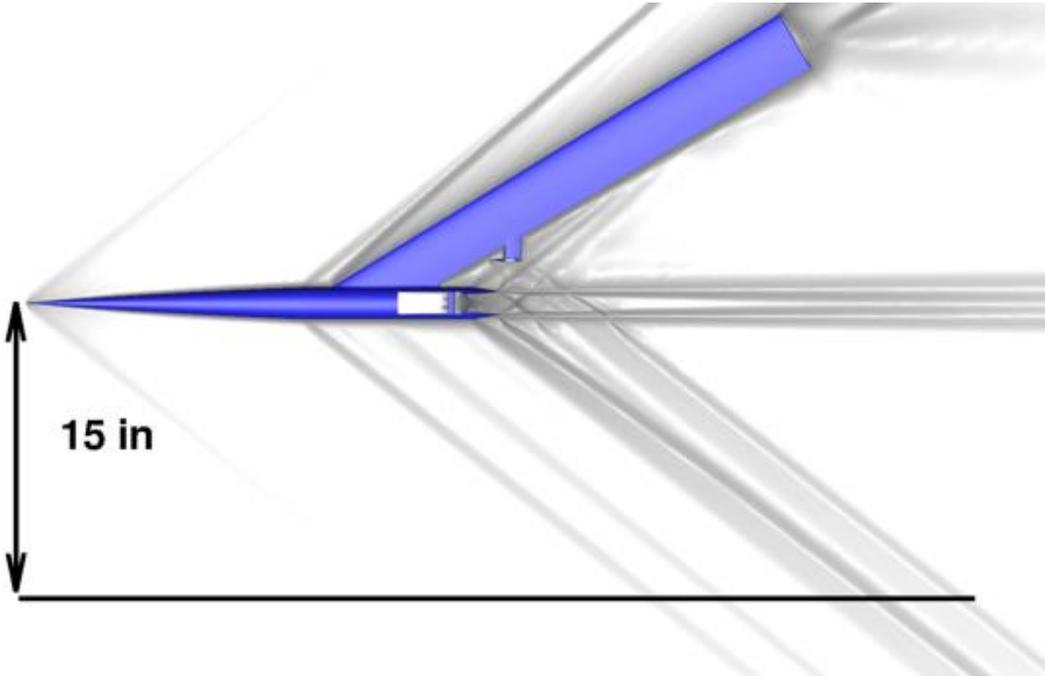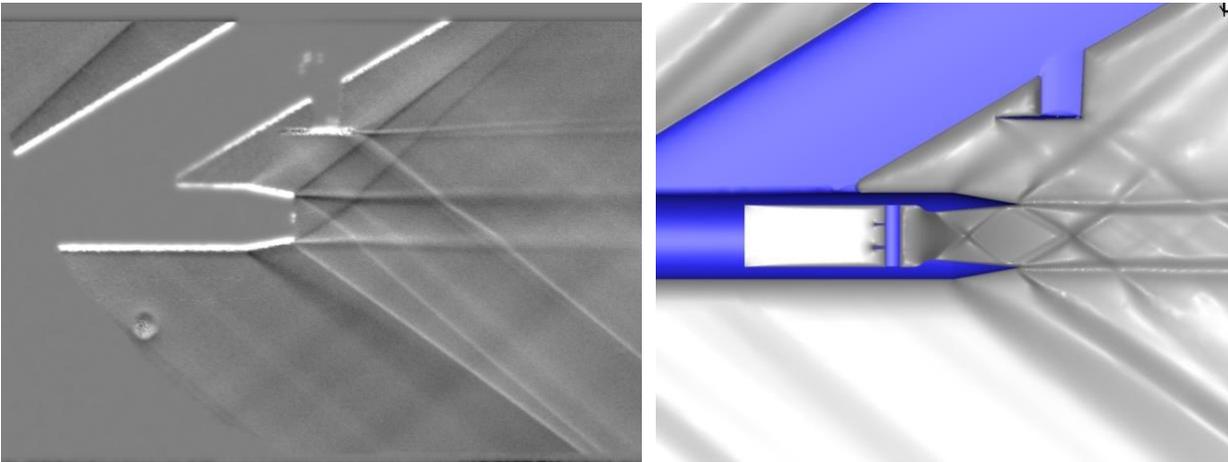

Figure 7 Symmetry plane biconvex model colored by USM3D-ME density gradient contours.

M_∞= 1.6, Re = 1.6, and Re = 376,850 per inch.

(a) RBOS *dY* image, *NPR* = 8, Ref. [17]   (b) USM3D-ME density gradient contours

Figure 8 Comparison of RBOS and USM3D-ME density gradient for the biconvex model.

Figure 9 shows a comparison of USM3D-ME on-track overpressure signatures for each of the grids given in Table 2. Figure 9 visually shows that the predicted overpressure signatures are grid converged. Figure 10 shows USM3D-ME off-track nearfield pressure signatures on the Bi_Tet_1 grid. The off-track signatures are in agreement on the front part of the body where the flow is compressive and in the axial direction. The blade perturbs the axial flow pattern and results in a slight shift in the off-track pressure signatures. The biconvex leading and trailing shocks slightly shift the off-track signatures from the on-track signature, just downstream of the lip-shock. Figure 11 shows a comparison of the USM3D-ME on-track overpressure signatures on the SBPW3 medium mixed-element and tetrahedral grids. The USM3D-ME signatures on both grids overlay. Figure 12 shows the comparison between USM3D-ME nearfield pressure signature and the mean signature of the solutions submitted by the SBPW3 participants. The USM3D-ME results are in excellent agreement with the mean signature.

In this study, the effect of three limiters on the nearfield overpressure signatures is investigated. Figure 13 shows the nearfield overpressure signatures predicted by USM3D-ME solutions computed with the Barth-Jespersen, Venkatakrishnan and van Albada limiters. The nearfield overpressure signature predicted by the three limiters are in good agreement in the front part of the signature, and predictions slightly differ in the aft part of the signature. The largest difference can be seen at and just downstream of the lip-shock, $X \sim 42.4$ in, and downstream of the trailing-edge shock, $X \sim 46.2$ in. Figure 13 depicts that the Venkatakrishnan limiter overpredicted the pressure rise of the nozzle lip shock and that the Barth-Jespersen limiter is more in agreement with the SBPW3 mean nearfield pressure signatures.
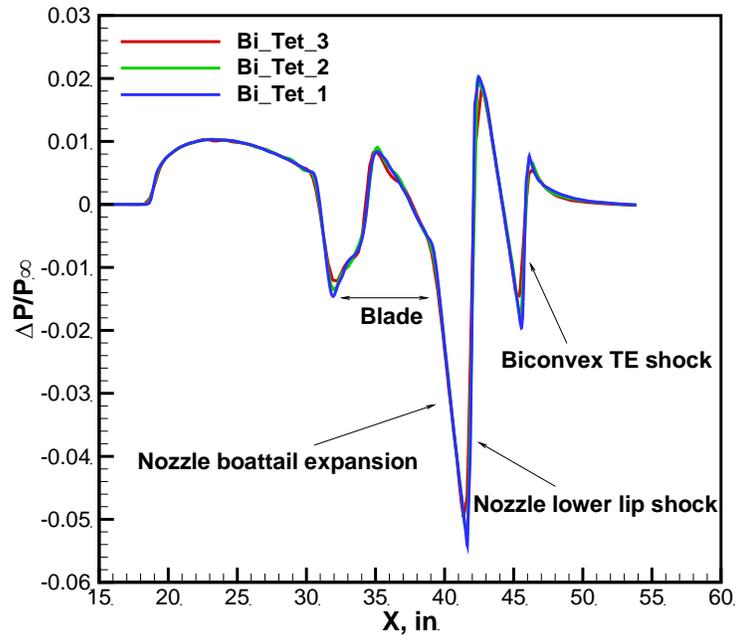
Figure 9 USM3D-ME nearfield overpressure signatures on the SBPW3 tetrahedral grids at $M_\infty = 1.6$, $\alpha = 0.0°$,
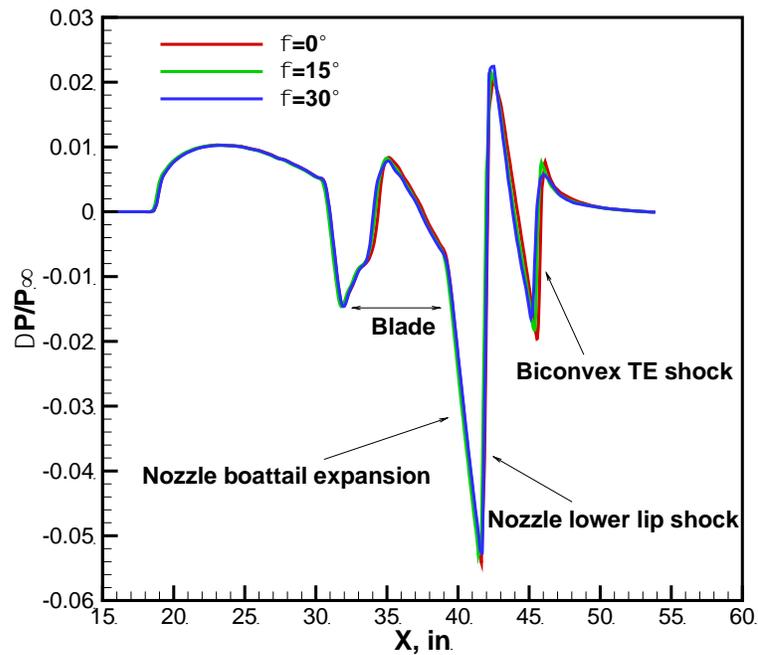**and** $Re = 376,850$ **per inch.**

Figure 10 USM3D-ME nearfield overpressure off-track signatures on the SBPW3 tetrahedral Bi_Tet_1 grid
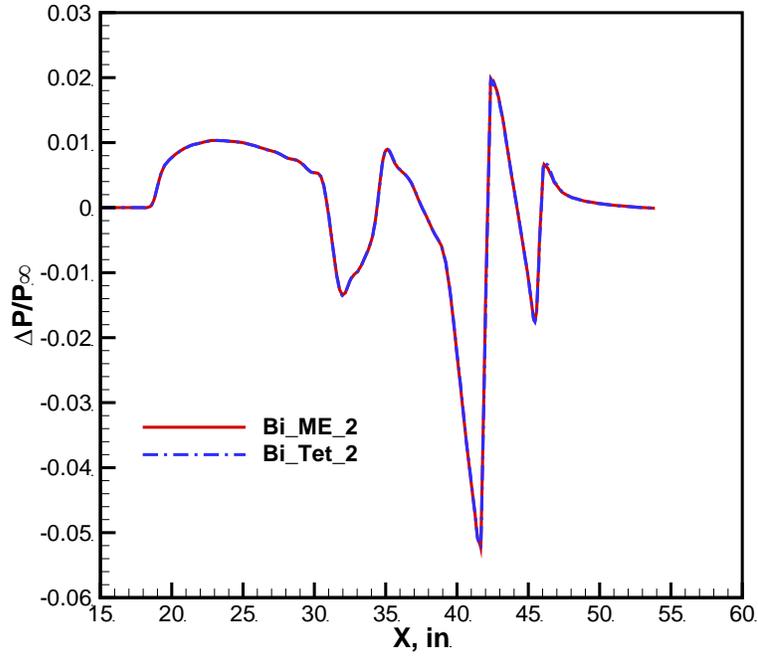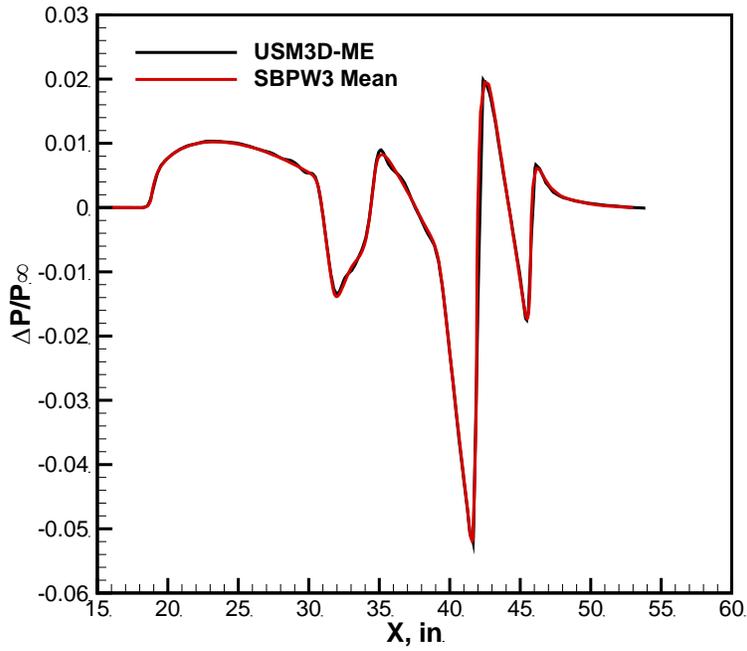**at** $M_\infty = 1.6$, $\alpha = 0.0°$, **and** $Re = 376,850$ **per inch.**

Figure 11 USM3D-ME nearfield overpressure signatures on the SBPW3 mixed-element and tetrahedral grids at $M_\infty = 1.6$, $\alpha = 0.0°$, and $Re = 376,850$ per inch.

Figure 12 Comparison of USM3D-ME nearfield pressure signatures with the SBPW3 participants' mean nearfield pressure signatures at $M_\infty = 1.6$, $\alpha = 0.0°$, and $Re = 376,850$ per inch.
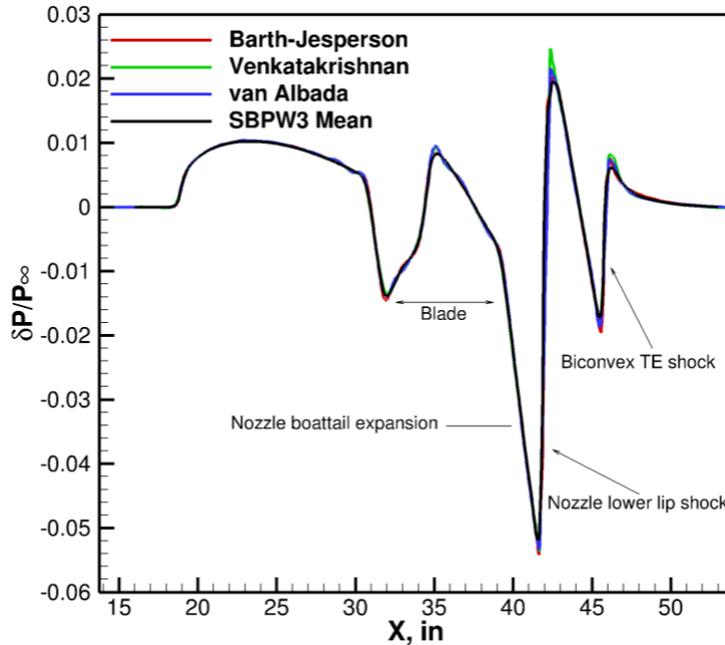
Figure 13 Effect of limiters on the nearfield overpressure signatures predicted by USM3D-ME at $M_\infty = 1.6$**,** $\alpha = 0.0°$**, and** $Re = 376{,}850$ **per inch.**

C608 Low Boom Flight Demonstrator

The C608 LBFD configuration is an early version of the NASA X-59 Low Boom Flight Demonstrator [31]. The C608 configuration is more representative of vehicles with lower ground loudness than the biconvex configuration. A schematic of the C608 configuration is given in Figure 2. USM3D-ME C608 simulations were conducted at $M_\infty = 1.4$, $\alpha = 0.0°$ and $Re = 109{,}776$ per inch. The nearfield overpressure signatures were extracted and propagated to the ground with the atmospheric propagation code, sBOOM.

The grids provided by the SBPW3 committee include a rotation of 2.15°, about the nose, to account for the C608 design angle of attack. USM3D-ME C608 simulations were performed on the SBPW3 mixed-element and tetrahedral grids. The simulations were conducted on the five coarsest grid levels. There was no need to compute simulations on the super-fine grid level as the solution was fully grid converged by the extrafine grid level, C608_ME_2 & C608_Tet_2. Simulations were also conducted on the in-house tetrahedral WF grids given in Table 5. The legacy USM3D code was used in the WF grid study.

Figure 14 shows USM3D-ME surface pressure coefficient contours for the C608 configuration. Figure 15 shows a close-up view of the Environment Control System (ECS). The shock emanating from the ECS vent wraps around the lower surface of the wing as shown by the red colored band. Figure 16 shows contours of nearfield overpressure signatures at three body length away from the C608. The black lines depict the location of the extracted pressure

signatures. The SBPW3 committee requested to extract off-track signatures every 2° up to $\varphi = 90°$ in the azimuthal direction, i.e., total of forty-five off-track angles.
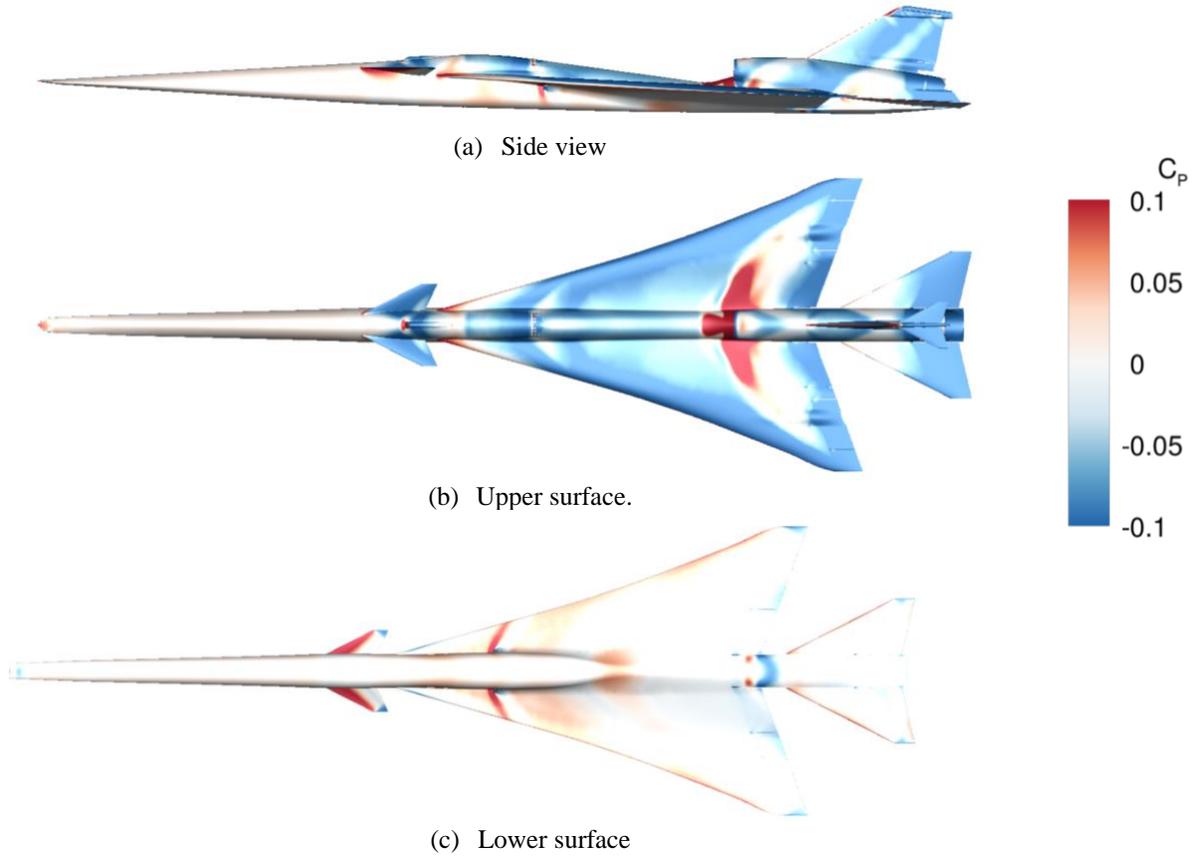

(a) Side view

(b) Upper surface.

(c) Lower surface

Figure 14 USM3D-ME surface pressure coefficient contours for the C608 at $M_\infty = 1.4$, $\alpha = 0.0°$, and $Re = 109,776$ per inch.
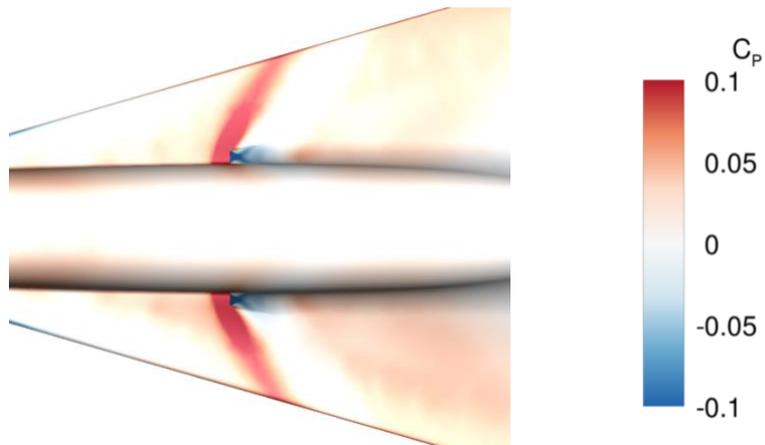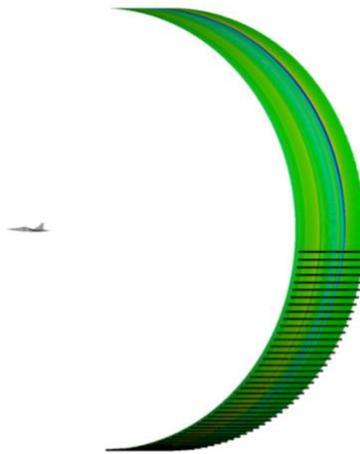

Figure 15 USM3D-ME surface pressure coefficient contours showing shock in front of the ECS at $M_\infty = 1.4$, $\alpha = 0.0°$, and $Re = 109,776$ per inch.

Figure 16 USM3D-ME computed overpressure contours at three body lengths away from the C608 at M_∞ = *1.4,* α *= 0.0°,* **and** Re *= 109,776 per inch.*

Figure 17a shows a comparison of USM3D-ME on-track overpressure signatures on the SBPW3 mixed-element grids. The overpressure signatures are grid converged on the C608_ME_2. The simulations on all grid levels capture consistently all flow features and shock locations. The nearfield pressure signatures extracted at three body length away from C608 configuration are propagated to the ground using sBOOM. Figure 17b shows the on-track ground signatures, with the corresponding PL noted in the legend. The C608 on-track ground signatures are grid converged. The difference in the PL levels between on-track ground signatures, computed from the USM3D-ME solutions on different grids, is less than 0.2 dB. Figure 17c shows the predicted carpets of PL. The solutions are grid converged. Discarding the results from the tiny grid level, the difference in the PL levels between the ground signatures is less than 1 dB, and the difference in PL computed on the fine and extrafine grid levels is less than 0.2 dB. All predicted nearfield overpressure, ground signatures, and corresponding PL levels have been uploaded to the SBPW3 website [10].
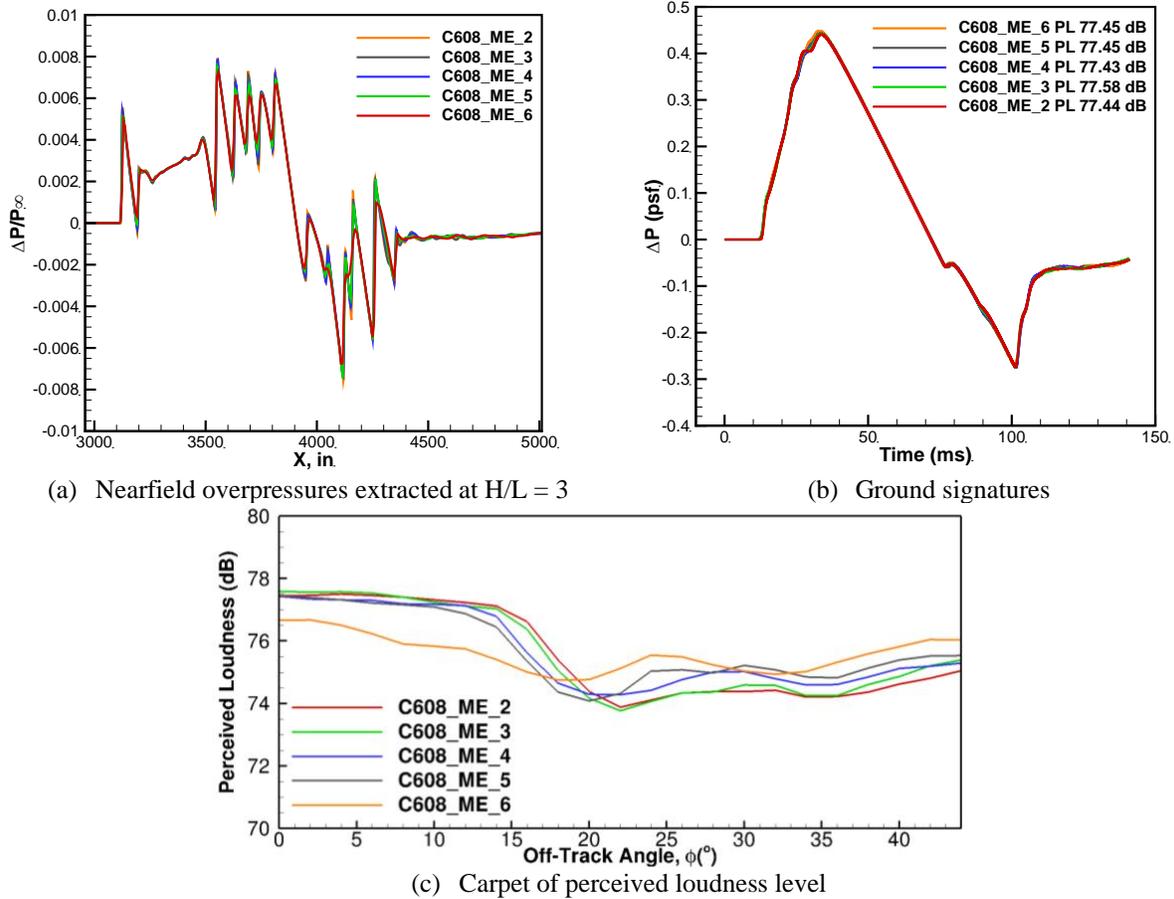
(a) Nearfield overpressures extracted at H/L = 3

(b) Ground signatures

(c) Carpet of perceived loudness level

Figure 17 USM3D-ME simulations for the C608 configuration on the SBPW3 mixed-element grids at $M_\infty = 1.4$, $\alpha = 0.0°$, and $Re = 109,776$ per inch.

Figure 18a shows comparisons of the USM3D-ME on-track nearfield overpressure signatures as predicted on the fine grid level of the mixed-element grid (C608_ME_3) and the tetrahedral grid (C608_TE_3), with the SBPW3 participants' mean. There is good agreement in capturing the shock locations between USM3D-ME on-track nearfield overpressure signatures and SBPW3 participants' mean, however, USM3D-ME solutions yield slightly stronger and sharper shocks. This should be expected since the mean is averaging several solutions and any peak would be rounded to some extent. Figure 18b shows the predicted PL levels on the ground. The front and aft part of the carpet shows good agreement between USM3D-ME predictions and the SBPW3 mean. The agreement deteriorates between off-track angles $12° < \varphi < 24°$. The bars shown in Fig. 18b are the one standard deviation of the SBPW3 ensemble data and they extend vertically from the mean. The carpet of predicted PLdB levels fell within one standard deviation band of the ensemble data mean.
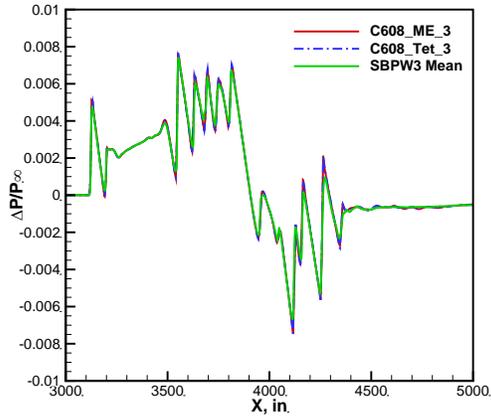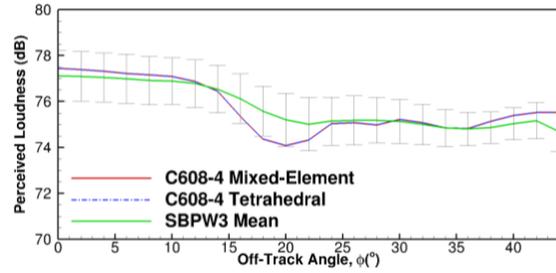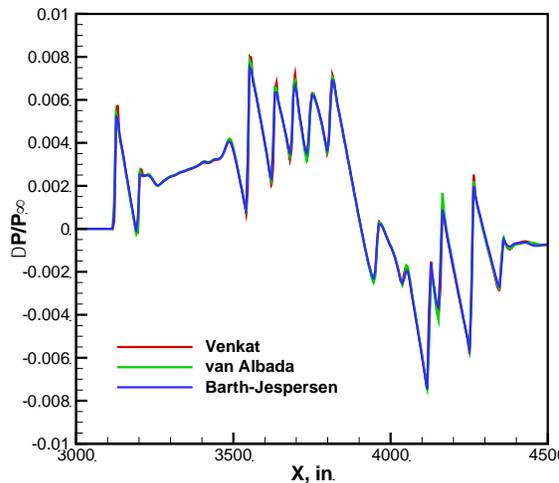
(a) Predicted nearfield overpressure signatures   (b) Carpet of predicted PL levels

Figure 18 Comparison between USM3D-ME predictions and SBPW3 mean at $M_\infty = 1.4$, $\alpha = 0.0°$, $H/L = 3$, and $Re = 109,776$ per inch.

The effect of limiters on the prediction of nearfield overpressure signature has been examined. The USM3D-ME solutions with Barth-Jespersen, Venkatakrishnan and van Albada limiters have been computed to predict the C608 nearfield overpressure signatures. Figure 19 shows on-track nearfield overpressure signatures as predicted on the extrafine grid level of the mixed-element grid (C608_ME_2). The signatures are in good agreement in terms of capturing the shock location, however, solutions with the different limiters yield different shock peaks. The Venkatakrishnan limiter has the least amount of dissipation and hence yield the highest shock peaks as compared to the van Albada and the Barth-Jespersen limiters. Figure 19b shows carpets of the PL levels as predicted by the solutions with the three limiters. The spread in PL values due to the use of different limiters is less than 0.2 dB.
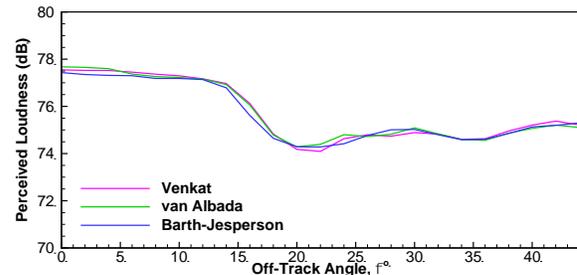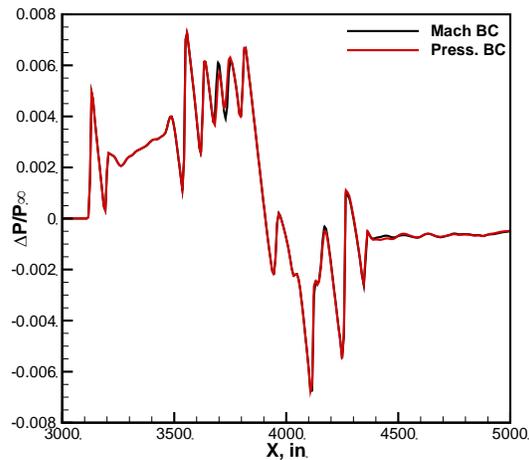

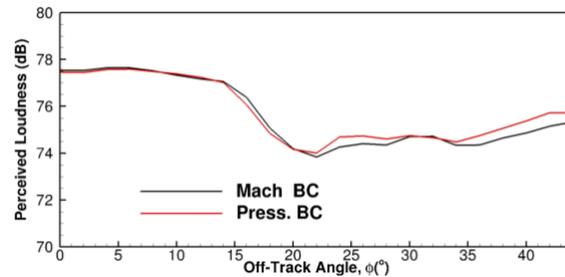(a) Predicted on-track nearfield overpressure signatures   (b) Carpet of predicted PLdB levels

Figure 19 Effect of limiters on USM3D-ME predictions at $M_\infty = 1.4$, $\alpha = 0.0°$, $H/L = 3$, and $Re = 109,776$ per inch.

The SBPW3 committee offered workshop participants two boundary condition (BC) types for the ECS inlet face and the engine fan face. Figure 20 shows the effect of specifying a prescribed Mach number at both faces, versus using a prescribed static pressure. The black line in Figure 20a depicts a signature with constant Mach number BC while the red line is a signature with a prescribed static pressure BC. The signatures are in good agreement with some discrepancy at around X ~ 3700 inches, which correlates with the ECS shock location. Figure 20a illustrates that the fan face BC type has little effect on the prediction of the on-track overpressure signature. This is probably due to the fact that any discrepancy in the flowfield due to the engine fan face BC is shielded by the C608 wing. Figure 20b shows the effect of BC type on the predictions of PL values on the ground. The PL values are in good agreement up to an off-track angle of ~ 22°. The spread in PL values due to the use of different BCs is less than 0.5 dB.
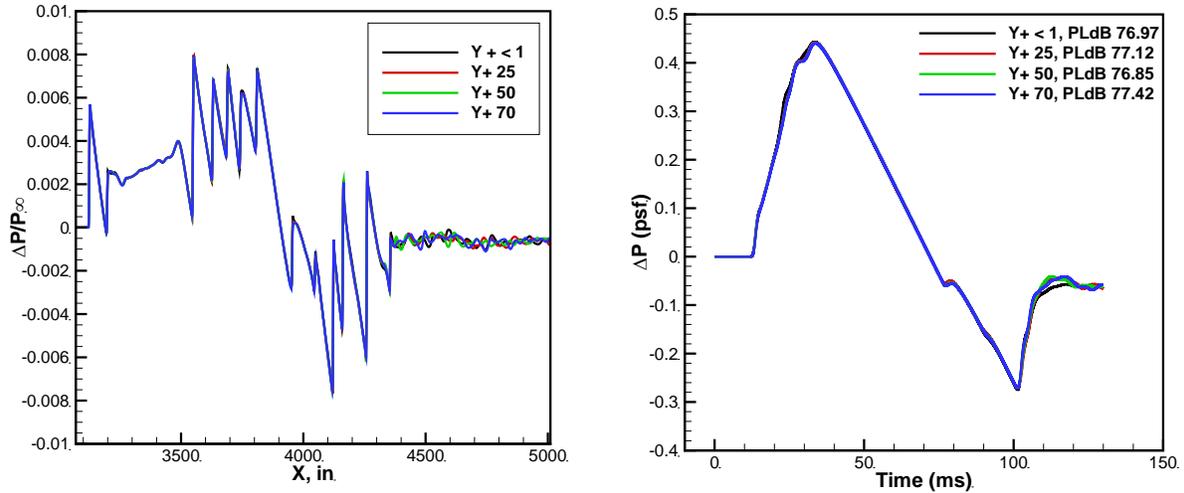

(a) Predicted on-track nearfield overpressure signatures

(b) Carpet of predicted PLdB levels

Figure 20 Effect of BC type on USM3D-ME predictions at $M_\infty = 1.4$, $\alpha = 0.0°$, $H/L = 3$, and $Re = 109,776$ per inch.

A study was conducted to examine the effectiveness of WF formulation in predicting nearfield overpressure signatures. The objective of the study was to assess whether a reduction in computing requirements (time to solution) could be achieved by using WF formulation while preserving the integrity of the signatures. A family of in-house grids were generated where y^+ varied from 0.1 to 70. The grid sourcing was the same on all four grids used in the WF study. The only difference between WF grids was in the first cell height. Details of the grids are provided in Table 5. The legacy USM3D code was used in the WF study. The Spalart-Allmaras one-equation model with the WF formulation was used to model turbulence on the grids, with $y^+ > 1$.

The nearfield overpressure signatures were extracted from the USM3D solutions, and the corresponding ground signatures and the PL values on the ground were computed and compared to the mean from the SBPW3 ensemble of data. Figure 21a shows the on-track nearfield overpressure signatures, extracted at three body-lengths away from the C608 configuration on the grids listed in Table 4. The front portion of the signatures are in good agreement with signatures overlayed on each other, however, discrepancies can be viewed at the aft part of the signature, plume region, at $X \geq 4300$ inches. Figure 21b shows the on-track C608 ground signatures propagated from the USM3D WF simulations. The comparison shows qualitatively good agreement with slight discrepancies from the predictions on the C608_WF_4 grid with $y^+ < 1$. The difference in perceived loudness level between on-track signatures, extracted from USM3D solutions, is less than 0.5 dB. Figure 20c shows comparisons between carpets of the PL values as predicted by USM3D WF simulations and the SBPW3 participants' mean. The spread in PL values is less than 1 dB and is within one standard deviation band of SBPW3 ensemble of data. The USM3D WF simulations provide a viable option to compute nearfield pressure signatures. Table 8 summarize the Central Processing Unit (CPU) time taken for WF simulations. A saving of almost 23% is observed in the CPU time required to converge WF RANS simulation on the C608_WF_1 grid as compared to the wall-resolved RANS simulation on the C608_WF_4 grid. However, if the interest is to compute the forces and moments as well as nearfield pressure signatures, grids with $y^+ < 1$ are recommended.

(a) Nearfield on-track overpressure signatures

(b) On-track ground signatures
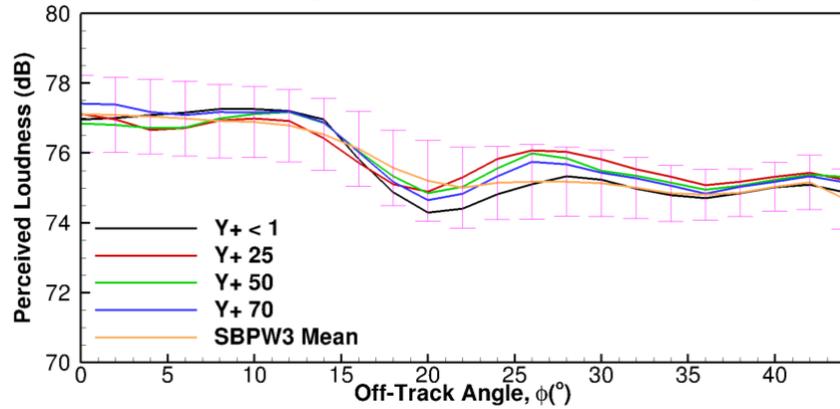
(c) Carpet of perceived loudness level

Figure 21 USM3D-ME C608 simulations on the wall function grids at $M_\infty = 1.4$, $\alpha = 0.0°$, H/L = 3, and Re = 109,776 per inch.

Table 8 Convergence time for the C608 wall function study.

Grid Level	y^+	Residual Reduction by Order of Magnitude	Time to Convergence sec/iteration/processor
C608_WF_4	70	4	0.879
C608_WF_3	50	4	0.95
C608_WF_2	25	4	1.14
C608_WF_1	< 1	4	1.14

V. Summary

This paper presented the USM3D results for the Third AIAA Sonic Boom Prediction Workshop (SBPW3) configurations. The SBPW3 configurations included a biconvex shock-plume interaction wind tunnel model and the NASA C608 low-boom aircraft. The USM3D-ME Navier–Stokes solver was used to compute the fully turbulent flow

around both configurations using the HLLC approximate Riemann solver for inviscid flux discretization and the negative variant of the Spalart-Allmaras turbulence model (SA-neg) to model turbulence.

USM3D-ME simulations for the biconvex model were conducted for a freestream Mach number of 1.6, and a unit Reynolds number of 376,850 per inch. The nearfield pressure signatures were extracted at distances of 15 inches away from the configuration and at three off-track angles, φ, of 0°, 15°, and 30°. The simulations were performed on mixed-element and tetrahedral grids provided by the SBPW3 committee. USM3D-ME biconvex solutions were grid converged. The nearfield pressure signatures were extracted and compared with the mean signature from the SBPW3 participants ensemble of data. The comparison showed excellent agreement.

USM3D-ME simulations for C608 were conducted for a freestream Mach number of 1.4, α of 2.15° and unit Reynolds number of 109,776 per inch. The nearfield pressure signatures were extracted at three body lengths away from the C608 configuration. The off-track signatures were extracted every 2° in the azimuthal direction, up to φ=90°. The simulations were performed on the mixed-element and the tetrahedral grids provided by the SBPW committee as well as on a family of grids generated by the in-house BoomGrid code. USM3D-ME solutions for the C608 configuration were grid converged. The predicted nearfield pressure signatures were propagated to the ground using the NASA propagation code sBOOM. The perceived loudness (PL) levels at the ground were computed by the LCASB loudness code. Good agreement was observed between the USM3D-ME predictions and the mean from the SBPW3 ensemble of data.

The Barth-Jesperson, Venkatakrishnan and van Albada limiters were used to evaluate the effect of limiters in predicting the turbulent flowfield for both the biconvex and C608 configurations. Predictions from solutions using the three limiters were in good agreement with the SBPW3 mean. The Venkatakrishnan limiter had the least amount of numerical dissipation and resulted in the strongest shocks. The Barth-Jesperson limiter was in a better agreement with the SBPW3 mean. All three limiters were within one standard deviation band of the SBPW3 ensemble of data.

A study was conducted to to assess the effect of using a wall-function (WF) formulation for sonic boom computations. A family of in-house tetrahedral grids were generated for this purpose, where y^+ varied from 0.1 to 70. The legacy tetrahedral USM3D code was used in the WF study. The nearfield pressure signatures were extracted from the USM3D solutions and the ground signature and the corresponding PL values on the ground were computed. The PL values predicted from the WF simulations were within one standard deviation band of the mean of the SBPW3 ensemble of data. WF simulations provided a viable option to compute nearfield pressure signatures. The WF approach

reduced computational time and yielded results equivalent to RANS simulations on near wall resolved grids with a y^+ < 1. However, if the interest is to compute forces and moments as well as nearfield pressure signatures, grids with y^+ < 1 are recommended.

Acknowledgments

References

[1] Park, M. A., and Morgenstern, J. M., "Summary and Statistical Analysis of the First AIAA Sonic Boom Prediction Workshop," AIAA Journal of Aircraft, Vol. 53, No. 2, 2016, pp. 578–598. doi:10.2514/1.C033449.

[2] AIAA Low Boom Prediction Workshop, Available: https://lbpw-ftp.larc.nasa.gov/lbpw1 [Accessed March 2020].

[3] AIAA Aviation 2014 Low Boom Special Session, Available: https://lbpw-ftp.larc.nasa.gov/aviation-2014 Accessed March 2020].

[4] AIAA Second Sonic Boom Workshop, Available: https://lbpw-ftp.larc.nasa.gov/sbpw2.

[5] Ueno, A., Kanamori, M., and Makino, Y., "Multi-fidelity Low-boom Design Based on Near-field Pressure Signature," AIAA Paper 2016–2033, 2016. https://doi.org/10.2514/6.2016-2033

[6] Wintzer, M., Ordaz, I., and Fenbert, J. W., "Under-Track CFD-Based Shape Optimization for a Low-Boom Demonstrator Concept", 33rd AIAA Applied Aerodynamics Conference, AIAA AVIATION Forum, AIAA 2015-2260. https://doi.org/10.2514/6.2015-2260

[7] Ordaz, I., Wintzer, M., and Rallabhandi, S. K., "Full-Carpet Design of a Low-Boom Demonstrator Concept", 33rd AIAA Applied Aerodynamics Conference, AIAA AVIATION Forum, AIAA 2015-2261. https://doi.org/10.2514/6.2015-2261

[8] Park, M. A., and Nemec, M., "Near Field Summary and Statistical Analysis of the Second AIAA Sonic Boom Prediction Workshop," AIAA Journal of Aircraft, Vol. 56, No. 3, 2019, pp. 851–875. doi:10.2514/1.C034866.

[9] Rallabhandi, S. K., and Loubeau, A., "Propagation Summary and Statistical Analysis of the Second AIAA Sonic Boom Prediction Workshop," AIAA Journal of Aircraft, Vol. 56, No. 3, 2019, pp. 876–895. doi:10.2514/1.C034805.

[10] Third Sonic Boom Workshop, Available: https://lbpw-ftp.larc.nasa.gov/sbpw3 [Accessed March 2020].

[11] Rallabhandi, S. K., and Loubeau, A., "Summary of Propagation Cases of the Third AIAA Sonic Boom Prediction Workshop," AIAA Paper 2021–229, 2021. doi:10.2514/6.2021-0229.

[12] Rallabhandi, S. K., "Propagation Analysis of the 3rd Sonic Boom Prediction Workshop Cases Using sBOOM," AIAA Paper 2021–230, 2021. doi:10.2514/6.2021-0230.

[13]   Carrier, G., Normand, P.-E., and Malbequi, P., "Analysis and Comparison of the Results of Two Tay Tracing-Based Sonic Boom Propagation Codes Applied to the SBPW3 Test Cases," AIAA Paper 2021–231, 2021. doi:10.2514/6.2021-0231.

[14]   Park, M. A., and Carter, M. B., "Nearfield Summary and Analysis of the Third AIAA Sonic Boom Prediction Workshop C608 Low Boom Demonstrator," AIAA Paper 2021–345, 2021. doi:10.2514/6.2021-0345.

[15]   Ishikawa, H., Koganezawa, S., and Makino, Y., "Near Field Sonic Boom Simulations for C608 Airplane of the Third AIAA SPW by Unstructured/Structured Overset Grid Method," AIAA Paper 2021–346, 2021. doi:10.2514/6.2021-0346.

[16]   Vanharen, J., Loseille, A., Alauzet, F., and Park, M. A., "Nearfield Anisotropic Mesh Adaptation for the Third AIAA Sonic Boom Workshop," AIAA Paper 2021–347, 2021. doi:10.2514/6.2021-0347.

[17]   Carter, M. B., and Park, M. A., "Near Field Summary and Analysis of the Third AIAA Sonic Boom Prediction Workshop Shock-Plume Interaction Case," AIAA Paper 2021–469, 2021. doi:10.2514/6.2021-0469.

[18]   Elmiligui, A., Pandya, M., Carter, M., Diskin, B., and Nayani, S., "USM3D Simulations for Third Sonic Boom Workshop," AIAA Paper 2021–470, 2021. doi:10.2514/6.2021-0470.

[19]   Duensing, J., Jensen, J., Housman, J., Piotrowski, M., Kenway, G., Maldonado, D., Sozer, E., and Kiris, C., "Structured Overset and Unstructured Grid Simulations for the Third AIAA Sonic Boom Prediction Workshop," AIAA Paper 2021–471, 2021. doi:10.2514/6.2021-0471.

[20]   Kirz, J., "DLR TAU Simulations for the Third AIAA Sonic Boom Prediction Workshop Near-Field Cases," AIAA Paper 2021–472, 2021. doi:10.2514/6.2021-0472.

[21]   Kassing, J., Carpenter, F. L., and Cizmas, P. G. A., "UNS3D Simulations for the Third Sonic Boom Prediction Workshop Part I: Biconvex 9x7 Shock-Plume Interaction Model," AIAA Paper 2020–2732, 2020. doi:10.2514/6.2020-2732.

[22]   Carpenter, F. L., and Cizmas, P. G. A., "UNS3D Simulations for the Third Sonic Boom Prediction Workshop Part II: C608 Low-Boom Flight Demonstrator," AIAA Paper 2020–2733, 2020. doi:10.2514/6.2020-2733.

[23]   Downs, R. S., Kaye, S., and Page, J. A., "Sonic Boom Prediction Workshop 3: Propagation Modeling using PCBoom," AIAA Paper 2020–2760, 2020. doi:10.2514/6.2020-2760.

[24]   Frink, N. T., Pirzadeh, S. Z, Parikh, P. C., Pandya, M. J., and Bhat, M. K., "The NASA Tetrahedral Unstructured Software System", The Aeronautical Journal, Vol. 104, No. 1040, October 2000, pp. 491-499.

[25]   Pandya, M. J., Frink, N. T., Ding, E., and Parlette, E. B., "Toward Verification of USM3D Extensions for Mixed Element Grids," AIAA Paper 2013-2541. https://doi.org/10.2514/6.2013-2541

[26]   Pandya, M. J., Diskin, B., Thomas, J. L., and Frink, N. T., "Improved Convergence and Robustness of USM3D Solutions on Mixed Element Grids," AIAA Journal, Vol. 54, No. 9, 2016, pp 2589-261 AIAA Journal, Vol. 54, No. 9, 2016, pp 2589-261.

[27]   Pandya, M. J., Diskin, B., Thomas, J. L., and Frink, N. T., "Assessment of USM3D Hierarchical Adaptive Nonlinear Iteration Method Preconditioners for Three Dimensional Cases," AIAA Journal, Vol. 55, No. 10, 2017, pp 3409-3424.

[28]   Pandya, M. J., Jespersen, D. C., Diskin, B., Thomas, J. L., and Frink, N. T., "Accuracy, Scalability, and Efficiency of Mixed-Element USM3D for Benchmark Three Dimensional Flows," AIAA Paper 2019-2333.

[29]   Durston, D. A., Cliff, S. E., Denison, M. F., Smith, N., Heineck, J. T., Schairer, E. T., Kushner, L. K., Castner, R. S., Elmiligui, A. A., Carter, M. B., Winski, C. S., Shea, P. R, and Blumenthal, B. T., "Nozzle Plume/Shock Interaction Sonic Boom Test Results from the NASA Ames 9- by 7-Foot Supersonic Wind Tunnel." AIAA 2017-0041, January 2017. https://doi.org/10.2514/6.2017-0041

[30]   Winski, C. S., Carter, M. B., Elmiligui, A. A., Pearl, J., Nayani, S., and Durston, D., "Computational and Experimental Study of Plume and Shock Interaction Effects on Sonic Boom in the NASA Ames 9x7 Supersonic Wind Tunnel." 2018 AIAA Aerospace Sciences Meeting, AIAA 2018-0331. https://doi.org/10.2514/6.2018-0331

[31]   NASA Low-Boom Flight Demonstration. https://www.nasa.gov/X59.

[32]   Harten, A., Lax, P. D., and van Leer, B., "On Upstream Differencing and Godunov-Type Scheme for Hyperbolic Conservation Laws," SIAM Review, Vol. 25, No. 1, 1983, p. 35.

[33]   Barth, T. J. and Jespersen, D. C., The design and application of upwind schemes on unstructured meshes, in: Proceedings of the 27th AIAA Aerospace Sciences Meeting, Reno, NV, Paper AIAA 89-0366, 1989.

[34]   Venkatakrishnan, V., Convergence to Steady State Solutions of the Euler Equations on Unstructured Grids with Limiters. Journal of Computational Physics, vol. 118, no. 1, 1995, pp. 120–130.

[35]   van Albada, G. D., van Leer, B., and Roberts, W. W., "A comparative study of computational methods in cosmic gas dynamics" Astronomy and Astrophysics, 108 (1982), pp. 76-84.

[36]   Spalart, P. R. and Allmaras, S. R., "A One-Equation Turbulence Model for Aerodynamic Flows," Recherche Aerospatiale, No. 1, 1994, pp. 5–21.

[37]   Allmaras, S. R., Johnson, F. T., and Spalart, P. R., "Modifications and Clarifications for the Implementation of the Spalart–Allmaras Turbulence Model," Seventh International Conference on Computational Fluid Dynamics, Paper ICCFD7-1902, Aug. 2012, http://www.iccfd.org/iccfd7/proceedings.html.

[38]   Rallabhandi, S. K., "Advanced Sonic Boom Prediction Using the Augmented Burgers Equation", Journal of Aircraft, Vol. 48, No. 4 (2011), pp. 1245-1253.

[39]   Stevens, S. S., "Perceived level of noise by Mark VII and decibels(E)," Journal of the acoustical society of America, Vol. 51, No. 2, 1972, pp. 575–601.

[40]   Shepherd, K. P. and Sullivan, B. M., "A Loudness Calculation Procedure Applied to Shaped Sonic Booms," NASA Technical Paper 3134, 1991.

[41]   Loubeau, A., Naka, Y., Cook, B. G., Sparrow, V. W., and Morgenstern, J. M., "A New Evaluation of Noise Metrics for Sonic Booms Using Existing Data," 2nd International Sonic Boom Forum, 20th International Symposium on Nonlinear Acoustics, July 2015.

[42]   HeldenMesh v3.0: https://heldenaero.com/heldenmesh.

[43]   Park, M. A., Campbell, R. L., Elmiligui, A. A., Cliff, S. E., and Nayani, S., "Specialized CFD Grid Generation Methods for Near-Field Sonic Boom Prediction" http://dx.doi.org/10.2514/6.2014-0115.

[44]   Hartwich, P. M. and Frink, N. T.: "Estimation of Propulsion Effects on Transonic Flows Over a Hypersonic Configuration", AIAA Paper 92-0523, January 6-9, 1992." https://doi.org/10.2514/6.1992-523